Journal of Solid State Chemistry 184 (2011) 655–666

Contents lists available at ScienceDirect

Journal of Solid State Chemistry

journal homepage: www.elsevier.com/locate/jssc

# Study of the surface chemistry and morphology of single walled carbon nanotube–magnetite composites

F. Marquez-Linares [a], O.N.C. Uwakweh [b], N. Lopez [c], E. Chavez [d], R. Polanco [a], C. Morant [e], J.M. Sanz [e], E. Elizalde [e], C. Neira [a], S. Nieto [a], R. Roque-Malherbe [a,*]

[a] Institute for Physical Chemical Applied Research, School of Science, University of Turabo, PO Box 3030, Gurabo, PR 00778-3030, USA
[b] Engineering Science and Materials Department, College of Engineering, University of Puerto Rico-Mayagüez Campus, Mayaguez, PR 00681-9044, USA
[c] Chemical Engineering Department, College of Engineering, University of Puerto Rico-Mayagüez Campus, Mayaguez, PR 00681-9000, USA
[d] Physics Department, University of Puerto Rico-Mayagüez Campus, Mayaguez, PR 00681-9000, USA
[e] Department of Applied Physics, C-XII, Universidad Autónoma de Madrid, Cantoblanco, 28049-Madrid, Spain

ARTICLE INFO

*Article history:*
Received 1 September 2010
Received in revised form
6 December 2010
Accepted 16 January 2011
Available online 27 January 2011

*Keywords:*
Carbon nanotubes
Magnetite
Composites
Mössbauer spectrometry
Surface chemistry

ABSTRACT

The study of the morphologies of the single walled carbon nanotube (SWCNT), magnetite nanoparticles (MNP), and the composite based on them was carried with combined X-ray diffraction (XRD), Raman spectroscopy (RS), scanning electron microscopy (SEM), field emission scanning electron microscopy (FESEM) and high resolution transmission electron microscopy (HRTEM). These techniques together with thermogravimetric analyses (TGA) and diffuse reflectance infrared transform spectroscopy (DRIFTS) confirmed the production of pure single phases, and that the composite material consisted of MNP attached to the outer surface of the SWCNT. The Mössbauer spectroscopy (MS) research showed the presence of a large quantity of Lewis acid sites in the highly dispersed magnetite particles supported on the SWCNT outer surface. The DRIFTS carbon dioxide adsorption study of the composites revealed significant adsorption of carbon dioxide, fundamentally in the Lewis acid sites. Then, the Lewis acid sites were observed to be catalytically active. Further, the electron exchange between the Lewis acid sites and the basic or amphoteric adsorbed molecules could influence the magnetic properties of the magnetite. Consequently, together with this first ever use of MS in the study of Lewis acid sites, this investigation revealed the potential of the composites for catalytic and sensors applications.



## 1. Introduction

Materials with a distinctive surface chemistry and morphology such as large surface area to volume ratio, activated surface atoms or sites and other features have applications in catalysis [1–7], adsorption [8–10] and other fields [11,12]. In particular, reactions catalyzed by acid and basic sites, located in the surface of solids, belong to the most important classes of heterogeneous catalytic conversions [1–7]. Usually, the exposed surfaces of these solid acids or bases have Brönsted acid or basic sites [1,2]. In other cases, coordinative unsaturated cations (cus) which are Lewis acid sites together with oxygen anions acting as Lewis basic sites may be observed [1,3,6].

The preparation of materials with a characteristic surface chemistry and morphology can be a complex task, more so when the characterization of the composition and structural features of the material under study, the detailed understanding of the surface chemistry and the morphology of the material under investigation is needed.

During the last decades, applying essentially: adsorption calorimetry, temperature-programmed desorption, temperature-programmed reduction, titration methods, infrared spectrometry, nuclear magnetic resonance, photoelectron spectroscopy, broad studies have been dedicated to the qualitative and quantitative description of the surface chemistry of materials [1,3,4,11,12].

Mössbauer spectrometry (MS) is an important research method for materials characterization [13–22]. However, it has not been, in comparison to other methods, extensively applied in the study of the surface chemistry of materials. This, comparatively, minor use of this method in catalysis studies is due to the fact that it application relevance is limited to phases containing those elements that exhibits the Mössbauer effect. In this regard, studies of catalytically active phases containing: iron [12–14,18–21], gold [17], ruthenium and tin [15] in its framework had been studied by Mössbauer spectrometry. It is accepted that correctly

* Corresponding author. Fax: +1 787 743 7979x4114.
*E-mail addresses:* RRoque@suagm.edu, RRoquemalh@aol.com (R. Roque-Malherbe).

0022-4596/$ - see front matter © 2011 Elsevier Inc. All rights reserved.
doi:10.1016/j.jssc.2011.01.017

interpreted Mössbauer spectra (MS) offers very useful information on: phase identification, determination of the oxidation state, structural information, particle size, kinetics of bulk transformation and lattice vibrations [12,16]. However, so far, to the best of our knowledge, the study of Lewis sites in iron containing materials has not been performed by Mössbauer spectroscopy.

In the research reported here the studied iron containing material is a single walled carbon nanotube (SWCNT)–magnetite composite. Given the fact that, in magnetite the iron sites which are exposed at the surface, are an electron accepting Lewis acid sites and the carbon nanotube stabilizes the magnetite nanoparticles, therefore, composite based on these materials would have potential practical applications.

The choice or selection of carbon nanotubes (CNTs) to support the active phase is based on their properties [23–40]. These carbon materials have features, such as, small diameters, in the order of the nanometers, relatively long lengths, in the order of micrometers, coupled with exceptional properties which include: excellent thermal conduction, outstanding structure-related electrical, optical, and high mechanical strength characteristics, high thermal and chemical stability, high-surface area and highly controlled pore size distribution [23,24]. Between these properties: high mechanical strength, high thermal steadiness, elevated chemical stability, high-surface area and highly controlled pore size distribution are exceptional properties of CNT's to be applied in the development of adsorbents [11,12,27], functionalized materials [28,29], catalyst supports [30–39] and catalysts [40]. All these reasons justify the application of single walled carbon nanotubes (SWCNTs) to produce composite materials.

Next the choice of magnetite as the active phase is predicated on the fact that it is one of the iron oxide phases that finds numerous applications due to its extraordinary properties [41–48]. Particularly, magnetite nanoparticles are widely applied as catalyst and catalytic precursors [49–53]. This oxide has also developed magnetic properties [54–58]. The catalytic properties are normally related to the presence of Lewis sites in the magnetite surface [52,53,59,60]. Besides, because magnetic properties are closely related to structural features [41,54–58]; we then suppose that the magnetic properties of the supported magnetite can be modified during adsorption of basic or amphoteric molecules in the electron accepting Lewis acid sites.

We have therefore synthesized composites, comprising of a SWCNT covalently functionalized with a capped magnetite nanoparticle, i.e., a magnetite core plus a capping organic material. Thereafter the capping material is detached, by heating, thereby producing thermally and chemically stable supported pure magnetite nanoparticles on the outer surface of the SWCNT. These materials were characterized by: X-ray diffraction (XRD), scanning electron microscopy (SEM), field emission scanning electron microscopy (FESEM), high resolution transmission electron microscopy (HRTEM), Raman spectroscopy (RS), and adsorption of nitrogen at 77 K. With thermal gravimetric analysis (TGA) and diffuse reflectance infrared Fourier transform spectrometry (DRIFTS) of the dehydrated materials the production of pure magnetite nanoparticles linked to the SWCNT outer surface was verified. Besides, a Mössbauer spectroscopy investigation, and a DRIFTS study of adsorbed carbon dioxide were carried out. Accordingly, the present paper has three major components; first, a marginal but necessary one, that is the: XRD, Raman, SEM and a careful nitrogen adsorption characterization of the composites. Second, the DRIFT study of the dehydrated composites and the TGA test of the composites, which were, as well, subsidiary but needed. The third part is the core of the paper, which is non-trivial, that is, the Mössbauer spectroscopy study of the Lewis acid sites at the magnetite surface and the corroboration of the Mössbauer findings by a DRIFTS study of the carbon dioxide adsorbed on the surface of the composite.

## 2. Materials and methods

### 2.1. Materials synthesis

All the consumed chemicals were analytical grade without additional purification. The water used in the synthesis process was triply distilled.

The synthesis of the vertically aligned single walled carbon nanotubes (SWCNTs), with high linearity and high density was based on the chemical vapor deposition (CVD) method on silicon and quartz surfaces. In order to grow the SWCNT the chemical vapor deposition (CVD) method was applied in a laboratory assembled facility [26]. This facility is a conventional thermal CVD system, composed of a three entry system, where, a cylindrical quartz reactor with an inner diameter of 25 mm and a length of 1 m was installed inside a tubular furnace. Substrates in a ceramic boat were introduced within the quartz reactor.

To produce the SWCNT, Co and Mo acetate solutions were deposited on the silicon and quartz substrates by dip-coating, following the procedure entailing the use of Co and Mo acetate diluted solutions namely $Co(CH_3COOH)_2 \cdot 4H_2O$ and $Mo(CH_3COOH)_2$ in absolute ethanol as catalyst sources. Typically for preparing 100 mL of the corresponding acetate solution 0.02 g of the Mo salt or 0.04 g of the Co salt was used. Both solutions were sonicated for 30 min and stirred for 2 h. Acetate solutions were kept in the dark to prevent photodecomposition. Silicon wafers (1 0 0) from El-CAT Inc., and fused quartz with both sides optically polished from SPI Supplies (quartz slide $25.4 \times 76\ mm^2$ super smooth) were employed as substrates. The substrates were cleaned with isopropyl alcohol and then dried in an oven at 70 °C before use. The dip-coating was made in two-steps, in which, the substrates were immersed into the acetate solutions and maintained there for about 10 s. As the first step, the substrates were immersed into the Mo acetate solution and subsequently calcined in an oven in air at about 400 °C for 20 min. Next, the substrates were cooled to room temperature and the dip-coating process repeated using the Co acetate solution. Further, the substrates were again calcined in an oven at 400 °C for 20 min. As a result, organics were removed from the surfaces and the metals subsequently oxidized. In the case of Mo, it formed an oxide layer that was expected to prevent the aggregation of the metallic Co particles formed during the CVD treatment that are responsible for the growth of SWNT [26].

Next, the system was closed and evacuated to $1 \times 10^{-2}$ Pa, with a mechanical pump. After 15 min the mechanical pump was stopped and a mixture of 90% $N_2$ and 10% $H_2$ gas was incorporated into the reactor (flow rate of 300 ml/min). Simultaneously, the reactor was heated up to 800 °C (10 °C $min^{-1}$). Upon reaching the synthesis temperature, the $N_2$–$H_2$ flow was stopped and a mixture of 10% $H_2$ and 90% $N_2$ with ethanol (99.5%) vaporized into the nitrogen stream, was introduced into the chamber at a flow rate of 200 ml/min. The growth time was about 5 min. The growth was finished by switching the gas to $N_2$ (300 ml/min) and cooling down the furnace. As a result, SWCNTs grouped in small bundles of ca. 20 were obtained [26].

In parallel, the magnetite nanoparticles were synthesized by the hydrothermal reaction of $(NH_4)_2Fe(SO_4)_2 \cdot 6H_2O$ in the presence of KOH in water solution. In a standard synthesis process [25], the initial step involved the preparation of 5 mmol of $(NH_4)_2Fe(SO_4)_2 \cdot 6H_2O$ that was dissolved in 100 mL of distilled water, after which this solution was added to another solution prepared with 30 mmol of KOH dissolved in 20 mL of distilled water and 2 mL of oleic acid dissolved in 40 mL of toluene. This mixture was added to the reaction solution. The hydrothermal treatment of the resulting solution was performed under reflux for 5 h at 100 °C. Subsequently, the product was cooled to room temperature and the organic phase containing the magnetite

nanoparticles was separated. Finally, the produced capped magnetite was precipitated with ethanol followed by centrifugation. The capped magnetite nanoparticles were cleaned with 0.5 M nitric acid and washed with a distilled water ethanol solution and then dried during 2 h at 70 °C.

The attachment of the capped magnetite nanoparticles on the SWCNT surface was based on the application of carboxylic acid pyrene derivative as a linker. This is a bi-functional molecule which can interact with the CNT through the $\pi$–$\pi$ stacking interactions between the pyrenil group and the CNT surface [25]. The linker was prepared by mixing 2 mmol of 1-pyrene carboxaldehyde with 2 mmol of 12-aminolauric acid in 40 mL of absolute ethanol. The mixture was stirred overnight at 40 °C and then filtered to separate the non-reacting solids. Thereafter, the reaction mixture was poured into a flask and roto-evaporated under vacuum.

The SWCNT were purified before use by refluxing at 100 °C in dilute nitric acid (2.3 mol/L) for 24 h to remove impurities. The solution was subsequently cooled and diluted with deionized water, thereafter the suspension was filtered and washed with water and ethanol and dried at 80 °C overnight [25].

The attachment of the magnetite nanoparticles was made by mixing 1 mmol of purified SWCNT and 10 mg of the carboxylic-pyrene derivative in 100 mL of chloroform. The solution was stirred overnight at room temperature and thereafter 10 mg of magnetite nanoparticles were added. This reaction mixture was stirred for 24 h and then filtered. The obtained solid was washed twice in ethanol at 70 °C and dried overnight at 60 °C [24]. The linkage between the capped nanoparticle and the carboxylic acid pyrene derivative linker is produced through the bonding of the carboxylate group of the linker.

### 2.2. X ray diffraction, Raman spectroscopy, nitrogen adsorption, scanning electron microscopy and field emission electron microscopy

The X-ray diffraction measurements were collected on a PANalytical X'Pert PRO diffractometer [25], in the case of magnetite-1 while with a Siemens D5000 X-ray Diffractometer, in the case of magnetite-2. Both equipment were positioned in vertical setup, corresponding to a, $\theta-2\theta$ geometry in the range: $5^\circ < 2\theta < 75^\circ$. Both equipment emitted Cu-$K\alpha$ radiation, filtered with a Ni foil and a Graphite monochromator.

The Raman spectra of the SWCNT-1 and magnetite-1, were recorded using a Confocal Raman Microscope (Renishaw RM2000) equipped with laser sources at 514, 633 and 785 nm, a Leica microscope and an electrically refrigerated CCD camera. The spectral resolution was set at 4 $cm^{-1}$, laser power employed was less than 10 mW and acquisition time of each spectrum was around 50 s. Additionally, the Raman spectra of the SWCNT-2 and magnetite-2, were measured with the help of a Jobin-Yvon T64000 spectrophotometer consisting of a double pre-monochromator coupled to a third monochromator/spectrograph with 1800 grooves/mm grating [61]. The 514.5 nm radiation of an Ar laser was focused in a less than 2 μm diameter circle area using Raman micro-probe with an 80× objective. The same microscope was used to collect the signal in backscattering geometry and to focus it at the entrance of the premonochromator [61]. The scattered light, dispersed by the spectrophotometer was detected by a charge coupled device detection system.

In order to measure the specific surface area, the pore volume and the pore size distribution (PSD) of the produced SWCNT were obtained, in a Quantachrome Autosorb-1 automatic physisorption analyzer, while adsorption, the isotherms of $N_2$ at 77 K in samples previously degassed at 573 K during 7 h in high vacuum ($10^{-6}$ Torr) [11,12]. With the help of the $N_2$ adsorption isotherms, the micropore volume, $W_{MP}$ [$cm^3/g$] was measured using the Dubinin method and the specific surface area, $S$ [$m^2/g$], applying the BET method [11]. The beginning of the adsorption isotherm was used for this purpose, i.e., $0.00001 < P/P_0 < 0.02$ for the Dubinin method and, $0.05 < P/P_0 < 0.3$, for the BET plot, where, $P$, is the equilibrium adsorption pressure, and, $P_0$, is the vapor pressure of the adsorbate at the temperature of the adsorption experiment [11]. For the calculation of the pore size distribution (PSD), the Saito and Foley ($S$–$F$) method was employed [12]. In order to compare the reported data with a commercial microporous material, the adsorption isotherm of $N_2$ at 77 K of the commercial zeolite Beta CP806 provided by ZEOLIST International was also measured with the Quantachrome Autosorb-1.

The scanning electron microscopy (SEM) study was carried out, with a JEOL CF 35 microscope in secondary electron mode at an accelerating voltage of 25 kV, to image the surface of the studied samples [25,26]. In addition to the use of JEOL CF35, a field emission SEM (FESEM) study was undertaken with a JOEL JM6400 microscope which enabled us to obtain high resolution images of the CNTs [25]. The surface morphology was revealed from SEM and FESEM images from which the average grain size was estimated, albeit qualitatively. The high resolution transmission electron microscopy images were recorded on a JEOL 3000 with an acceleration voltage of 300 kV.

### 2.3. Thermogravimetric analysis and diffuse reflectance Fourier transform infrared spectrometry

The TGA testing process was carried out with a TA, Q-500 equipment. In this facility were also prepared the non-capped magnetite nanoparticles (magnetite cores detached from the capping materials) supported on a SWCNT. To make the TGA test, the samples were placed into a ceramic sample holder, which was suspended from an analytical balance [12]. Next, the sample holder was heated according to a predetermined thermal cycle, which consisted of ramping temperature in a linear scan, from 23 to 700 °C, at a heating rate of 5 °C/min, in a flow of 100 ml/min of the purge gas that was pure $N_2$. The data collection, the temperature control, the programmed heating rate, and the gas flow control, were all automatically controlled with the TA software for the TQ500 TGA. The TGA data was collected as a Wt [%] versus $T$ [°C] profile, where the $Wt\% = (M_t/M_0)100$, is the per-cent ratio of the sample mass during the thermal treatment. In the expression, $M_t$, is the sample mass and $M_0$ is the initial mass of the sample.

To get the diffuse reflectance infrared Fourier transform spectra (DRIFTS), a Thermo Scientific Nicolet iS10 FTIR spectrometer with the Smart Collector for diffuse reflectance analysis and the environmental chamber for the smart collector was used. The spectra were collected with a resolution of 4 $cm^{-1}$ and were made with 100 scans per sample. To get the sample spectrum in the case of the dehydrated samples, a background with KBr (FTIR pure, provided by Nicolet) located in the sample holder of the environmental chamber was made by applying the same conditions used to get, later, the dehydrated sample spectra. To dehydrate the samples, they were heated, at 150 °C, under $N_2$ (Praxair, 99.99%) flowing at a rate of 50 cc/min for 2 h. Lastly, the spectra of the dehydrated composites were obtained with the sample inside the environmental chamber, at room temperature, under $N_2$ (Praxair, 99.99%) flowing at a rate of 50 cc/min.

### 2.4. Mössbauer spectroscopy and DRIFTS study of adsorbed carbon dioxide

The room temperature Mössbauer spectroscopy (MS) measurements were carried out with a SEECo supplied spectrometer operating at constant acceleration mode with a 50 mCi $^{57}Co$ gamma-ray source in a Rh matrix made by Rietverc GmbH. The velocity scale was chosen to ensure a thorough scan of the

materials in order to reveal all the features associated with the magnetic and non-magnetic portions of the sample material. The 1024 point raw data were folded and analyzed using WMOSS, a public domain Mossbauer spectral analysis Program available at www.SEECo.us, which was formerly WEBRES Company. The calibration was made with reference to α-Fe metal, while the fitting was done based on the Rancourt Hyperfine distribution model [62].

To get the DRIFTS spectrum of carbon dioxide adsorbed at room temperature on the composite surface a Thermo Scientific Nicolet iS10 FTIR spectrometer with the Smart Collector for diffuse reflectance analysis and the environmental chamber for the smart collector was used. The spectra were collected with a resolution of 4 $cm^{-1}$ and were generated by 100 scans per sample. The background taken, in this case, was the composite sample dehydrated at 300 °C and cooled to room temperature under $N_2$ (Praxair, 99.99%) flow. Thereafter, a flow of $CO_2$ (Praxair, 99.99%) at a rate of 50 cc/min during 3 min was carried out. Following this step, the samples were purged under $N_2$ flow at a rate of 50 cc/min during 1 min. Finally, the spectrum was obtained with the sample inside the environmental chamber, at room temperature in order to get the DRIFTS profile of the carbon dioxide molecule adsorbed on the composite surface.

## 3. Results and discussion

### 3.1. X-ray diffraction, Raman spectrometry, nitrogen adsorption, scanning electron microscopy and field emission scanning electron microscopy, phase, structural and morphological analysis

The XRD powder diffraction profile of magnetite-1 [25], showed that it was a highly crystalline material, when compared with the diffraction patterns contained in the International Center for Diffraction Data Powder Diffraction File™ database, and as well, when evaluated against literature data [56]. Besides, there was no other crystalline phase detected.

Fig. 1 shows the XRD diffraction pattern of magnetite-2. It was evident that this is a poorly crystallized material. However it exhibited some peaks corresponding to the magnetite phase. The average particle size, of magnetite-2 (see Table 1), was determined with the help of the Scherrer's formula [63]:

$$\phi = \frac{0.9\lambda}{\Delta(2\theta_B)\cos\theta_B} \quad (1)$$

where $\phi$ is the crystallite size or particle diameter (P.D.); $\lambda = 1.5418$ Å is the $K\alpha$ weighted average wavelength of Cu;

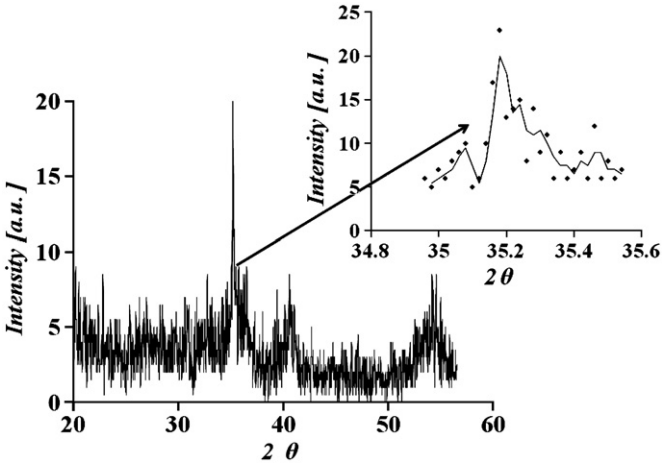


**Fig. 1.** XRD of magnetite-2, with the detail of the peak at 35.18°.

**Table 1**
Parameters measured with the help of the nitrogen adsorption data and SEM.

| Sample | S ($m^2g^{-1}$) | $W_{MP}^{Du}$ ($cm^3g^{-1}$) | $W_{MP}^{SF}$ ($cm^3g^{-1}$) | $D_{mode}^{SF}$ (nm) | $\phi$ (nm) |
|---|---|---|---|---|---|
| SWCNT-1 | 530 (BET) | 0.22 | 0.22 | 1.3 | *NA* |
| SWCNT-2 | 500 (BET) | 0.21 | 0.21 | 1.2 | *NA* |
| $Fe_3O_4$-1 | 230 (SEM-P.D.) | ≈0 | ≈0 | *NA* | 5 |
| $Fe_3O_4$-2 | 380 (XRD-P.D.) | ≈0 | ≈0 | *NA* | 3 |
| *Zeolite Beta (CP806)* | 660 (BET) | 0.25 | *0.27* | *0.6* | *NA* |

*Note*: The acronym P.D. means that the area of the magnetites was calculated with the help of Eq. (2).

$\Delta(2\theta_B)$, is the angular half-width of the Bragg peak whose angular position is, $\theta_B$, possible to calculate the average P.D ($\phi$). The small particle size, measured, $\phi = 3 \pm 2$ nm, could be the cause of the low quality of the XRD profile.

Now, with the value reported for the P.D. it was possible to estimate the magnetite-2 surface area with the help of the following relation:

$$S = \frac{6}{\phi\rho} \quad (2)$$

where $\phi$ is the crystallite size and $\rho$ is the magnetite density. Since: $\phi = 3 \pm 2$ nm and $\rho = 5.15$ g/$cm^3$ is the magnetite density; then, the specific surface, $S$, is around: 380 $m^2$/g (see Table 1).

It is necessary here to acknowledge that the previously reported parameters are associated with the magnetite core of the capped material. Based on this premise it could be assumed, from the previously reported data, that the magnetite-2 core was a highly dispersed material, because of its high specific surface area.

Raman spectroscopy is a powerful tool to analyze the structure of materials [64]. In particular, the vibration modes in carbon nanotubes, which are excited by Raman spectroscopy, have a particular significance, since the obtained spectrum differs as a function of the diameter of the carbon nanotube owing to modifications with size [25]. The analysis of Raman spectra of carbon nanotubes was based on phonon dispersion in two-dimensional graphite. In this regard, the most important Raman dispersion bands in carbon nanotubes in the range analyzed in the present study [65–68] are: 1550–1600 $cm^{-1}$ and 1250–1450 $cm^{-1}$, where the first band is the graphite band (*G*-band), produced from the high degree of symmetry and order of $sp^2$ carbon materials, and the second band was the disorder-induced phonon mode (*D*-band) [65], produced by the presence of defects in the structure of the $sp^2$ carbon [66]. Additionally the Radial Breathing Modes (RBMs) modes [67] were also present in the low frequency Raman shift. Since, the room temperature Raman spectra of both SWCNT-1 [26] and SWCNT-2 were very similar, therefore the spectrum of the SWCNT-2 only is reported in Fig. 2.

Both spectra showed the most intense and characteristic bands in the frequency range of 1250–1600 $cm^{-1}$ and a low frequency shift region dominated by a band at 180–280 $cm^{-1}$. Since, the *G*-band is located at around 1594 $cm^{-1}$ and the *D*-band at around 1296 $cm^{-1}$ and the RBMs modes are located, approximately, between 180 and 280 $cm^{-1}$ [65–68]; therefore, these peaks precisely confirmed the existence of carbon nanotubes in the tested sample.

In addition, the high value of the *G*/*D* intensity ratio clearly point to SWCNTs of high purity [26]. The Raman shift of the different RBMs of the SWCNTs was correlated with the diameter of the SWCNT, using the following empirical formula [67], $d = 248/\nu_{RBM}$, where $\nu_{RBM}$ is the corresponding wavenumber ($cm^{-1}$) and $d$ is the diameter of the SWCNT in nm. The diameter

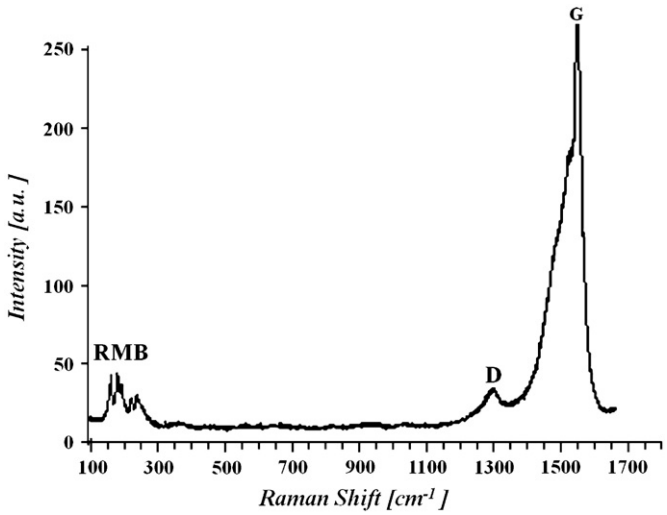


**Fig. 2.** Raman dispersion spectrum of SWCNT-2.

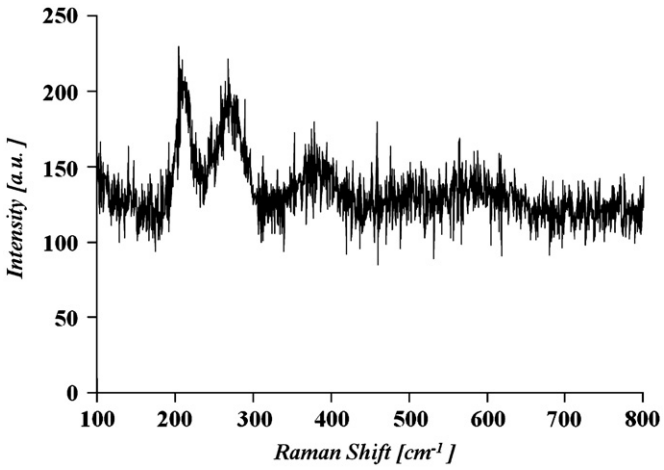


**Fig. 3.** Raman dispersion spectrum of magnetite-2.

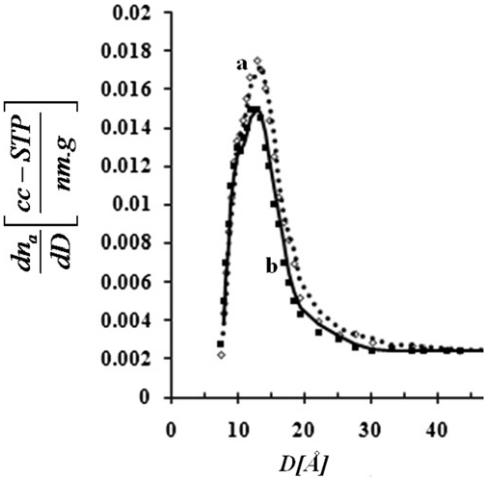


**Fig. 4.** Saito–Foley pore size distribution of SWCNT-1 (a) and SWCNT-1 (b).

determined by this approximation, showed a narrow distribution ranging from 0.9 to 1.2 nm that agreed with the dimensions measured by adsorption (see below).

Magnetite is a mixed $Fe^{2+}$ and $Fe^{3+}$ oxide with an inverse spinel structure. The spinel structure can be designated as: $(Me^{2+}_{1-\lambda}Fe^{3+}_{\lambda})[Me^{2+}_{\lambda}Fe^{3+}_{2-\lambda}]O_4$; where $\lambda$ quantify the degree of inversion, and the regular parenthesis ($A$ sites) and square brackets ($B$ sites) refer to the tetrahedral and octahedral sites, respectively. When $\lambda=1$, we have the inverse spinel, and for $\lambda=0$, we have the normal spinel while the case for $\lambda=2/3$ correspond to a completely random distribution [49]. The magnetite inverse-spinel structure belongs to the cubic space group $Fd3m4$. In this structure the complete unit cell enclose 56 atoms. However, the smallest Bravais cell contains 14 atoms; implying that there are 42 vibrational modes [69]. The factor-group analysis method [64] predicts five Raman-active modes; that is: $A_{1g}+1E_{g1}+3T_{2g}$ [69]. In this regard, a Raman spectrum of magnetite nanoparticles shows normally characteristic peaks around 670–535 $cm^{-1}$, since normally the active Raman bands in nanocrystals are shifted [70]. These band corresponds to the intramolecular $A_{1g}$ mode, which involves the stretching vibrations of the oxygen atoms along the Fe($A$)–O bonds and one of the $T_{2g}$; since, the three $T_{2g}$ modes have bands around [69]. Then the bands in the frequency range 550–700 $cm^{-1}$ precisely characterize magnetite nanoparticles [71]. The room temperature Raman spectrum of the synthesized magnetite-1 [25], is a normal spectrum of this material, since it showed the main bands in the frequency range of 550–700 $cm^{-1}$, consequently, this spectrum confirmed that magnetite-1 was well crystallized. The magnetite-2 sample Raman spectrum is very diffuse (see Fig. 3) and only showed minute bands in the frequency range of 200–300 $cm^{-1}$. This fact was correlated with the very small particle size of the magnetite, since during the interaction of the Laser with small crystalline particles, the structure is somewhat broken.

Gas adsorption measurements are widely applied in the characterization of the surface chemistry and morphology of porous materials [11,12], since the adsorbate explores the porosity of materials, thereby permitting the calculation of different parameters. In this regard, the specific surface area is typically measured by means of the BET method [11,12], while the micropore volume is usually measured using the $t$-plot method [11], the Dubinin adsorption isotherm or the Langmuir type isotherm equation for micropore volume filling [11,12]. The pore size distribution (PSD) in the micropore range is calculated generally with the help of the Horvath–Kawazoe methodology [11], particularly in the case of cylindrical pores with the help of the Saito–Foley method [12].

In order to apply real adsorption data to the BET isotherm equation, it is customary to use the BET equation in linear form in the region of, $0.05 < x < 0.4$, of the isotherm, where $x=P/P_0$ is the relation between the adsorption equilibrium pressure, $P$, and the vapor pressure, $P_0$ at 77 K of $N_2$, which in the present case is the adsorbate. Thus, the specific surface area was calculated for all the tested samples by means of the linear BET plot, which made possible the computation of the BET surface area, i.e., $S^{BET}$ (see Table 1).

Adsorption in the micropores is the main method applied for the measurement of the microporous volume, by means of the Dubinin linear plot [12] and, as well the linear plot of the Langmuir type isotherm for volume filling [11]. In the present case the Dubinin type linear plots were applied to the adsorption data taken from the isotherm in the range: $0.0001 < x < 0.1$. Thereafter, the Gurvich rule was applied for the calculation of the Dubinin micropore volume, $W^{Du}_{MP}$, (see Table 1).

The Saito–Foley pore size distribution (SF–PSD) of the synthesized SWCNT materials are shown in Fig. 4, while the maximum cumulative pore volume, $W^{SF}_{MP}$, and mode of the SF–PSD distribution, $D^{SF}_{mode}$,which measure the size of the pore of the nanotubes, are reported in Table 1 for the SWCNT-1 and SWCNT-2 samples. The adsorption data displayed in Table 1 demonstrated that the

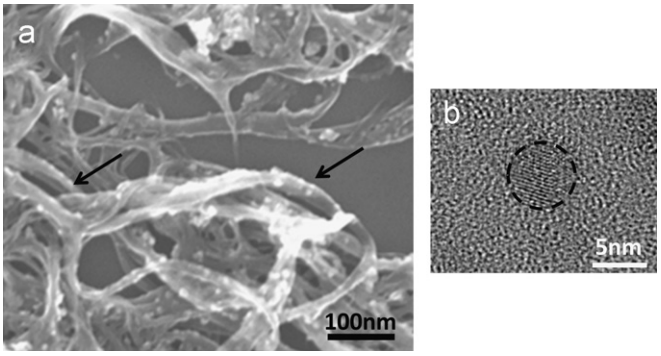


**Fig. 5.** FESEM (a) and HRTEM (b) images of the SWCNT–magnetite-1 composite and an isolated magnetite nanoparticle, respectively.

studied SWCNTs exhibited a relatively large specific surface area and a fairly large micropore volume, which is approximately equal to the micropore volume of a Beta zeolite (see Table 1).

Further, the calculated pore size distributions (PSD) indicates that the synthesized SWCNT have a distribution of pores with a clear, and highly populated, maximum at 1.2–1.3 nm, which was consistent with the Raman results.

The adsorption data, as well, showed the absence of mesoporosity in the sample. That is, the adsorption data indicates that the adsorption space of the obtained SWCNT's are completely in the micropore region, exhibiting a relatively high micropore volume, specifically, 0.22 $cm^3/g$, which is similar to those of a very important commercial microporous material, explicitly , the zeolite Beta (see Table 1). Additionally these SWCNT materials showed a high BET specific surface area of approximately 550 $m^2/g$, which is also similar to the BET surface area of the zeolite Beta. However, the pore size of the SWCNT is double than those reported for zeolite Beta (see Table 1).

It is then possible to infer, from the adsorption data, that the obtained SWCNTs have high specific surface area, developed microporosity and homogeneous pore size. Consequently, taking into account the thermal and chemical stability of SWCNT, the synthesized materials could be considered as good supports for catalytically active phases.

Fig. 5a, shows the field emission scanning electron microscopy (FESEM) image of the composite material containing magentite-1 showing evidently the attached magnetite nanoparticles (indicated by arrows). Fig. 5 presents the HRTEM image of an isolated magnetite nanoparticle whose diameter is ca. 5 nm.

The FESEM and scanning electron microscopy (SEM) data of magnetite-1, showed that the nanoparticles have an average particle diameter [25] (P.D), $\phi \approx 5 \pm 2$ nm. With the previously reported P.D. data, it was possible to estimate the magnetite-1 surface area, with the help of Eq. (2). Subsequently, the specific surface area was calculated as, $S = 230\ m^2/g$ (see Table 1). It is necessary to recognize that the parameters measured with SEM are related with the magnetite core of the capped material and consequently means that we have a material with a large specific surface area and highly dispersed.

### *3.2. Thermogravimetric analysis (TGA) and diffuse reflectance Fourier transform spectroscopy (DRIFTS) study of the dehydrated samples*

The TGA profiles reported in this section were taken under $N_2$ flow, in order to avoid magnetite oxidation. The thermal gravimetric profile of the capped magnetite-1 is shown in Fig. 6a. This profile shows at low temperature very small weight losses, since the thermal process only comprise the removal of weakly linked

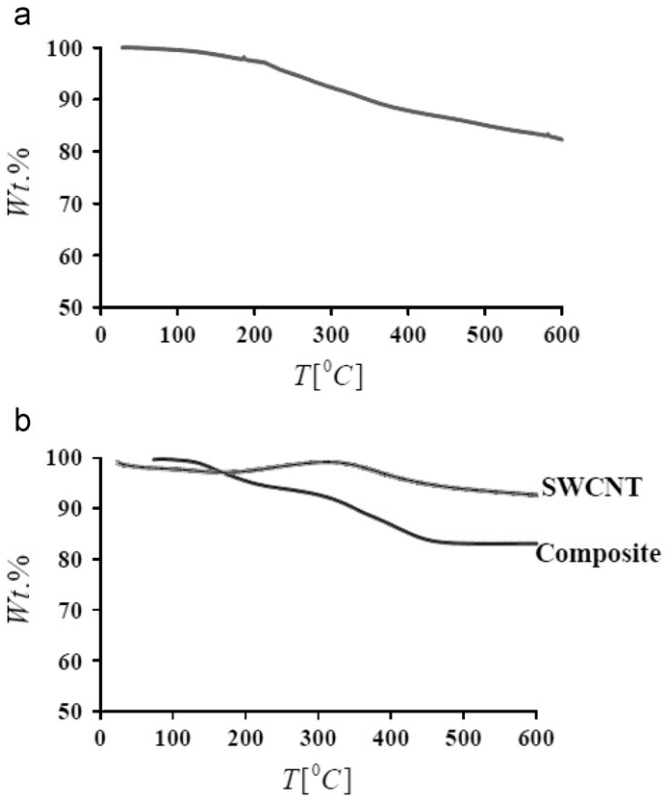


**Fig. 6.** TGA profile of the capped magnetite-1 nanoparticles (a) the SWCNT-1 and the composite-1.

physically adsorbed water. When the temperature was increased to more elevated temperatures, i.e., $T > 200\ ^\circ C$, the observed weight losses were noteworthy. This weight loss was related to desorption and decomposition of the organic surfactant present on the magnetite surface [58]. The thermal gravimetric profiles of the SWCNT-1 and the composite-1 are shown in Fig. 6b. In this case, at low temperature, the weight losses were very small for both samples, given that, during the thermal process at this temperature, only weakly adsorbed water was desorbed. At higher temperatures, i.e., $T > 200\ ^\circ C$, the SWCNT profile did not show noticeable effects. In contrast, the composite profile shows (Fig. 6b) desorption and decomposition of the organic phase attached on the magnetite surface [58]. That is, above 200 °C the linker and the surfactants were detached from the SWCNT. It is necessary to recognize now that while the weight loss curve of the composite at high temperature (Fig. 6b) is plain, the same curve (Fig. 6a) in the case of the capped magnetite is not completely plain, it is slowly diminishing. This fact can be related with the presence of the SWCNT support, in the composite case.

In the present TGA study, the attachment of the organic surfactant compound on the magnetite nanoparticle surface was confirmed. Furthermore, it also showed the detachment of the organic surfactant capping material and the linker from the magnetite particle attached to the SWCNT surface. These facts pointed to the fact that it is possible to support a pure magnetite core in a SWCNT. To confirm this we will apply DRIFTS.

The DRIFT spectra of the magnetite calcined at 900 °C were recorded while the samples were included in the environmental chamber at room temperature, and after heating it at 150 °C under $N_2$ flow for 2 h, also, inside the environmental chamber, in order to remove adsorbed water. In Fig. 7a the DRIFT spectra of the calcined magnetite-1 and composite-1 in the range between 475 and 1000 $cm^{-1}$ are shown. The presence of cores of

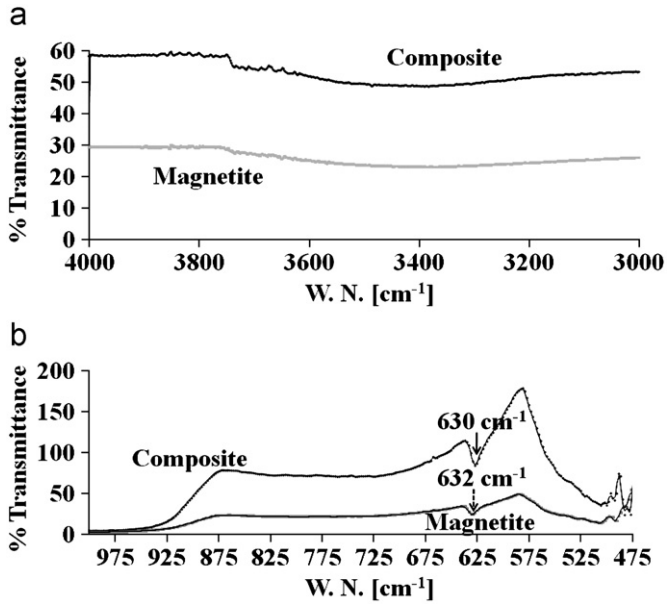


**Fig. 7.** DRIFTS spectra of the calcined magnetite-1 and the calcined SWCNT-1–magnetite-1 composite in the region between 475 and 2000 $cm^{-1}$ (a) and in the 3000 and 4000 $cm^{-1}$.

magnetite nanoparticles in the tested samples was evidenced by the strong band at around 630–632 $cm^{-1}$ that can be assigned to the $\nu$(FeO) stretching mode [72,73]. This fact means that the magnetite cores were detached from the SWCNT after calcination at 900 °C. The spectra displayed in Fig. 7b revealed that both samples were totally dehydroxilated during the calcination process. It was also evident that the whole DRIFT spectra showed that the heat treatment removed the capping organic material, since no bands form organic compounds were found. Consequently, were obtained nanoparticles of non-capped, magnetite. Fact, recognized by the shifting of the $\nu$(FeO) stretching band to the region around 630 $cm^{-1}$. This vibration, in the case of bulk magnetite, is located at around 570 $cm^{-1}$, and for magnetite nanoparticles in the region around 630 $cm^{-1}$ [72].

The previous results confirmed that it is possible to support a highly dispersed magnetite in a SWCNT with high specific surface, micropore volume and a homogeneous pore size.

### 3.3. Mössbauer investigation

Fig. 8a shows the magnetite-1 Mössbauer spectrum (MS). Additionally, in Table 2 are reported the isomer shift, the quadrupole splitting, the internal magnetic field, and the relative areas of the different sub-spectra related with the nucleus of $^{57}$Fe located in different sites, which in combination shape the experimental spectrum, and were revealed with the help of the fitting, with the WMOSS Mössbauer spectral analysis program, of the experimental spectrum applying the Rancourt hyperfine distribution model [62]. Also, to be definite it is necessary to state that the calibration was made with reference to α-Fe metal.

The room temperature (298 K), $^{57}$Fe Mössbauer spectrum of bulk magnetite shows two sextets. The first one has a hyperfine magnetic field, $B_{hf}$=48.8 T, and an isomer shift, relative to α-Fe, $\delta_A$=0.27 mm/s; assigned to $Fe^{3+}$ ions; the second sextet has a, $B_{hf}$=45.7 T, and $\delta_B$=0.65 mm/s; this sextet correspond to the mixed $Fe^{2+}$–$Fe^{3+}$ ions [55]. As a consequence of the cubic structure of bulk magnetite the previously mentioned sextets shows a negligible quadrupole splitting, i.e. $\Delta_A \approx \Delta_B \approx 0$ mm/s. But, in the case of magnetite nanoparticles, the surface is very

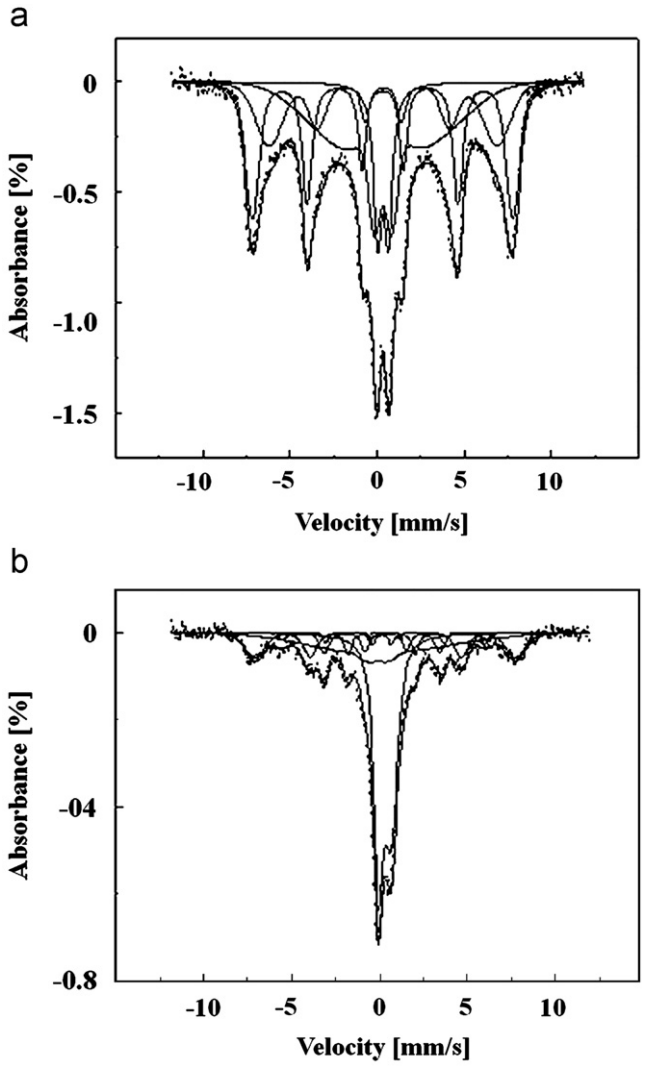


**Fig. 8.** Mössbauer spectra of magnetite-1 (a) and the SWCNT–magnetite-1 composite (b).

**Table 2**
Mossbauer parameters for the magnetite-1 nanoparticles.

| Sites | RA (%) | I.S., $\delta$ (mm/s) | Q.S., $\Delta$ (mm/s) | I.M.F, $B_{hf}$ (T) |
|---|---|---|---|---|
| Site-1 | 11.2 | 0.354 | 0.682 | |
| Site-2 | 41.0 | 0.394 | 0.087 | 18.8 |
| Site-3 | 18.8 | 0.359 | −0.022 | 40.7 |
| Site-4 | 29.0 | 0.326 | 0.0015 | 46.2 |

developed. Therefore, in the surface of the iron oxide, the termination of the bulk phase implies the rupture of the cubic environment for the iron cations present in the magnetite structure. Subsequently, should be observed a quadrupole splitting effect on account of the presence of part of the iron cations in the surface of the oxide particles. Where, because of the damaged cubic symmetry these iron cations are immersed in a non-zero electric field gradient which produces the quadrupole splitting [12].

Additionally, in the case of magnetite nanoparticles its size could be so small that every particle turns out to be a single magnetic domain. The consequence of this arrangement is superparamagnetism [56–58]. In this case the Fe nucleus involved in

the Mössbauer experiment experiences an averaged zero effective internal magnetic field, and consequently doublet or singlet spectra are obtained, depending on the existence of quadrupole splitting or not, respectively [57,58].

It is evident that the reported room temperature spectrum of the synthesized capped magnetite nanoparticles (Fig. 8a) does not look like the spectrum of bulk magnetite. Fig. 8a displays magnetite-1 spectrum, composed of a central portion with a prominent doublet with the peaks around the center of the spectrum, a somewhat distorted sextet, and two clear magnetic sextet peaks indicative of magnetic order associated with some of the material's constituents. In this spectrum, the overall line broadening associated with the peaks was a result of particle size distribution. The central portion contribution was readily associated with the phenomenon of superparamagnetic relaxation related to the small particles size of the cores of the capped magnetite nanoparticles. In this regard, for magnetite, it has been reported that the particle size limit to observe the superparamagnetic behavior should be less than 10 nm [54,74]. Therefore, about 11% of the synthesized nanoparticles had particle diameter less than 10 nm, since, as shown in Table 2, the superparamagentic doublet was fitted with an isomer shift ($\delta$) of 0.354 mm/s, a quadrupole splitting ($\Delta$) of 0.682 mm/s, with a relative abundance (R.A.) accounting for 11.2% of the total spectrum. The quadrupole splitting can be related to a structure with symmetry less than cubic. However, magnetite crystallizes in a cubic structure. Therefore, the superparamagnetic relaxation should be observed as a single line, i.e., without quadrupole splitting. Thereafter, the observed splitting effect can be only justified on account of the presence of part of the $^{57}$Fe atoms in the surface of the nanoparticles, because of the high specific surface of these nanoparticles (see Table 1), where the broken cubic symmetry causes that these atoms are immersed in a non-zero electric field gradient [74], producing quadrupole splitting. These iron cations located in the surface are essentially Lewis sites [52,59]. Additionally, at the surface, are also located oxygen anions which can operate as electron donating Lewis base sites [60].

One of the sextets fitted to the experimental spectrum (site 2), that is, those for the Fe site with the least internal magnetic field, showed an isomer shift ($\delta$) of 0.394 mm/s, a quadrupole splitting ($\Delta$) of 0.087 mm/s and internal magnetic field ($B_{hf}$) 18.8 T, and a relative abundance (R.A.) of 41.0% of the total spectrum. Thus, it was the most populated site. The above alluded sextet exhibited a very low internal magnetic field, possible for magnetite nanoparticles [54], as a consequence of the fluctuations through an angle $\theta$ of the field acting around the magnetic easy axes in a nanoparticle [57]. Thereafter, this broad sextet is connected to a relaxation processes, and thus related to nanoparticles of diameter around 10 nm. Consequently: 52.2%=41.0%+11.2% of the particles have diameters between4 and 10 nm. Where, the non-uniform particle size distribution could explain varying cationic distribution which also influences the magnetic properties [56].

The other two sextets fitted to the experimental spectrum showed isomer shifts ($\delta$), quadrupole splitting, and internal magnetic field, respectively as, $\delta_B$=0.359 mm/s, and $\delta_A$=0.326 mm/s, $\Delta_B$=−0.022 mm/s, and $\Delta_A$=0.0015 mm/s; $B^B_{hf}$=40.7 T and $B^A_{hf}$=46.2 T, and a relative abundance (R.A.) of 18.8% and 29.0% of the total spectrum, respectively. These two sites (octahedral and tetrahedral sites) corresponded to 37. 8% of the iron located in the magnetite nanoparticles. The decrease of the internal magnetic field of these sextets with respect to the bulk magnetite is normal for magnetic nanoparticles. The Fe located in the previously described octahedral and tetrahedral sites corresponds to particles bigger than 10 nm. Additionally, this Fe is located in the bulk, because of the lack of quadrupole splitting.

The results of the previous discussion of the Mössbauer spectrum of magentite-1 are in accordance with the HRTEM and SEM data, which showed that the nanoparticles have an average particle diameter (P.D), $\phi \approx 5 \pm 2$ nm.

Fig. 8b shows the SWCNT-1–magnetite-1 composite MS. In Table 3 are reported the isomer shift, the quadrupole splitting, the internal magnetic field, and the relative area of the different spectra related with the nucleus of $^{57}$Fe located in diverse sites, which in conjunction form the experimental spectrum, and were revealed as was previously described. The room temperature MS of the SWCNT-1–magnetite-1 was revealed composed of a segment in the center of the spectrum which shows a large highly asymmetric doublet, two somewhat distorted sextets and two clear magnetic sextet peaks. In this spectrum, the sextet peaks were found broader, fewer intense and less well resolved than in the magnetite-1 spectrum. This fact revealed more intense interactions associated with cationic distribution. Also is revealed an overall line broadening associated with the peaks, which was as well a result of particle size and cationic distribution. The central portion part of the spectrum was also associated with the particle size related superparamagnetism, that is, particles with less than 10 nm of particle diameter. As shown in Table 3, the superparamagnetic doublet was fitted with an isomer shift ($\delta$) of 0.307 mm/s, a quadrupole splitting ($\Delta$) of 0.735 mm/s, with a relative abundance (R.A.) of 47.9% of the total spectrum. As displayed in Table 2, the superparamagnetic doublet of magnetite-1 was fitted with an isomer shift ($\delta$) of 0.354 mm/s, a quadrupole splitting ($\Delta$) of 0.682 mm/s. Consequently, it was observed an increase in the isomer shift of 0.047 mm/s, and a decrease of the quadrupole splitting of – 0.053 mm/s, which could be considered as part of the error in the determination of these parameters. Then, in essence it is the same site previously found in the magnetite nanoparticles, but more populated, indicating more iron in the surface of the particle. This composite when it was treated with heat under nitrogen flow and the magnetite was converted into a non-capped magnetite, i.e., was transformed in a material highly populated by Lewis sites.

Two of the sextets fitted to the experimental spectrum (sites 2 and 3), that is those for the Fe site with the least internal magnetic field, shows isomer shifts ($\delta$) of: 0.121 mm/s and 0.142 mm/s, quadrupole splittings ($\Delta$) of 0.412 mm/s and 0.0609 mm/s and internal magnetic field ($B_{hf}$) 21.9 T and 36.1 T, and relative abundances (R.A.) of 24.6% and 2.4% of the total spectrum. These low internal magnetic field broad sextets, as was commented for this type of site in the magnetite, were related to the superparamagnetic relaxation process. Then, this iron is located in small particles. One of these sextets exhibiting a noticeable quadrupole splitting, was also related with iron in the surface. Thereafter in the composite about 72% (see Table 3) of the iron is located in the surface as cus, that is, are Lewis acid sites.

The other two sextets fitted to the experimental spectrum shows isomer shifts ($\delta$) quadrupole splittings, and internal magnetic field, respectively thus, $\delta_B$=0.285 mm/s and $\delta_A$=0.345 mm/s; $\Delta$=−0.061 mm/s and $\Delta$=0.025 mm/s; $B^B_{hf}$=36.1 T and $B^A_{hf}$=45.9 T, and a relative abundance (R.A.) of 17.5% and 7.6% of the total

**Table 3**
Mossbauer parameters for the composite SWCNT-1–magnetite-1.

| Sites | RA (%) | I.S., $\delta$ (mm/s) | Q.S., $\Delta$ (mm/s) | I.M.F, $B_{hf}$ (T) |
|---|---|---|---|---|
| Site-1 | 47.9 | 0.307 | 0.735 | |
| Site-2 | 24.6 | 0.121 | 0.412 | 21.9 |
| Site-3 | 2.4 | 0.285 | −0.0609 | 36.1 |
| Site-4 | 17.5 | 0.345 | −0.0254 | 45.9 |
| Site-5 | 7.6 | 0.142 | 0.01136 | 20.4 |

spectrum. Both sextets were related to Fe placed, correspondingly, in the octahedral ($B$) and tetrahedral ($A$) sites. In this case also the reduction of the internal magnetic field with respect to the bulk magnetite was an effect usual for magnetic nanoparticles as was previously explained. These sextets are related with bigger particles and iron located in the bulk, because of the absence of quadrupole splitting.

One important feature of the MS of the composite was related to the fact that the spectrum shown in Fig. 8b in comparison to those reported in Fig. 8a, clearly showed, the development of peak asymmetry effect, which are recognized as two major effects affecting the relative line intensities of the hyperfine pattern of a polycrystalline material, that is, texture and lattice vibrational anisotropy, also known as the Goldanskii–Karyagin effect [75]. It is necessary to remark that it is difficult to distinguish between both effects [75,76]. In the present case this asymmetry effect was suggestive of interactions involving electronic exchange, which provoked a texturing effect in the magnetite nanoparticles. This effect was due to the linking of the capped magnetite to the SWCNT, fact indicative of an interaction between the magnetite and the SWCNT. Furthermore, these sextet peaks were broader and less well resolved than in the capped magnetite, instance that revealed interactions associated with cationic distribution.

The magnetite-2 spectrum displayed in Fig. 9a was fitted with five Fe-sites. The corresponding parameters are listed in Table 4.

The spectrum was well resolved with the prominent central doublet clearly discernable. However, the magnetic peaks were rather broad. The central part could be immediately related with a superparamagnetic effect related to the small particles size of the capped magnetite nanoparticles. That is about 35% of the synthesized nanoparticles have particle diameter less than 10 nm; since the superparamagnetic doublet was fitted with an isomer shift ($\delta$) of 0.363 mm/s, a quadrupole splitting ($\Delta$) of 0.622 mm/s, with a relative abundance (R.A.) accounting for 34.87% of the total spectrum (see Table 4). The calculated quadrupole splitting was linked, as in the case of magnetite-1 with the presence of a fraction of the $^{57}$Fe atoms in the surface of the nanoparticles, on account of the high specific surface of these nanoparticles (see Table 1). These iron sites, placed in the surface are Lewis acid sites [52,59]. In addition oxygen anions located at this surface, acts as electron donating Lewis base sites, furthermore in particular situations hydroxyl groups which acts as Brönsted sites are also formed [60].

The sextets fitted to the experimental spectrum are broad not intense and poorly resolved indicating that the particles are minute and feebly crystallized. Consequently, the results of the previous discussion of the Mössbauer spectrum of magnetite-2 are in harmony with the XRD and Raman data.

The SWCNT–magnetite-2 composite MS shown in Fig. 9b, displayed a prominent central doublet and poorly resolved magnetic peaks. The corresponding parameters are listed in Table 5. The most important feature of this spectrum was the segment in the center where a large doublet was shown. This central portion of the spectrum was associated to superparamagnetism, related to particle size. As shown in Table 5, the superparamagnetic doublet was fitted with an isomer shift ($\delta$) of 0.311 mm/s, a quadrupole splitting ($\Delta$) of 0.515 mm/s, with a relative abundance (R.A.) of 34.72% of the total spectrum. As displayed in Table 3, the superparamagnetic doublet of composite-1, in essence, was very similar to the present doublet, which was also highly asymmetric. Therefore, the iron site represented by this doublet, during calcination, while takes place the releasing of the organic surfactant and the linker become a Lewis acid site in the surface [59]. The sextets fitted to the experimental spectrum are so bad resolved that could be related to small particles.

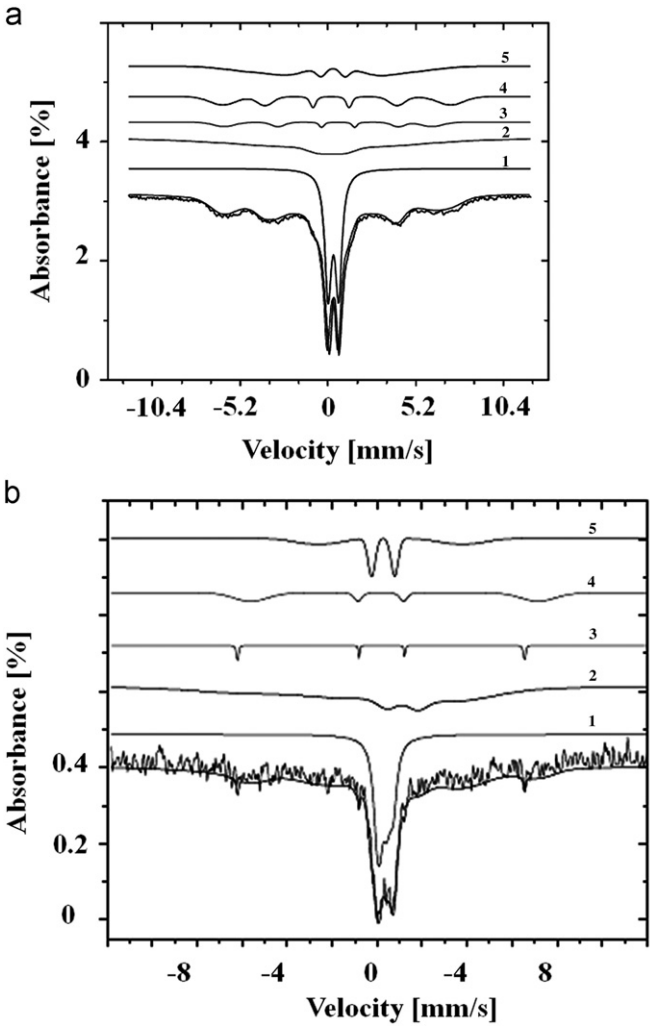


**Fig. 9.** Mössbauer spectra of magnetite-2 (a) and the SWCNT–magnetite-2 composite (b).

**Table 4**
Mossbauer parameters for magnetite-2.

| Sites | RA (%) | I.S., $\delta$ (mm/s) | Q.S., $\Delta$ (mm/s) | I.M.F, $B_{hf}$ (T) |
|---|---|---|---|---|
| Site-1 | 34.87 | 0.363 | 0.622 | 0.17 |
| Site-2 | 27.88 | 0.001 | −0.498 | 28.17 |
| Site-3 | 5.88 | 0.345 | −0.602 | 38.06 |
| Site-4 | 13.50 | 0.393 | 0.333 | 41.75 |
| Site-5 | 17.87 | 0.289 | −0.105 | 27,56 |

**Table 5**
Mossbauer parameters for the SWCNT–magnetite-2 composite.

| Sites | RA (%) | I.S., $\delta$ (mm/s) | Q.S., $\Delta$ (mm/s) | I.M.F, $B_{hf}$ (T) |
|---|---|---|---|---|
| Site-1 | 34.72 | 0.311 | 0.515 | 0.88 |
| Site-2 | 39.89 | 0.001 | −2.240 | 25.75 |
| Site-3 | 1.47 | 0.188 | −0.0399 | 39.46 |
| Site-4 | 9.60 | 0.465 | 0.607 | 39.48 |
| Site-5 | 14.32 | 0.422 | 0.310 | 19.95 |

The development of the peak asymmetry effect is related essentially to texture and lattice vibrational anisotropy [75,76]. In the present case, as also was noted for the composite-1 this

asymmetry effect, was indicative of interactions involving electronic exchange, that cause a texturing effect in the magnetite nanoparticles. This effect was caused by the linking of the capped magnetite to the SWCNT.

The Mössbauer experiments showed that a considerable amount of the iron present in the magnetite nanoparticles (see the % in Tables 2–5) were located in the surface of the iron oxide. These iron cations are coordinatively unsaturated cations (cus), that is, Lewis acid sites; additionally, the oxygen anions accompanying these iron cations are Lewis basic sites [1,3,6]. As a result, with the help of Mössbauer spectrometry was provided adequate indications of the existence of Lewis acid and basic sites in the tested samples.

### 3.4. DRIFTS study of the adsorption of carbon dioxide in the composite

A significant application of carbon dioxide adsorption as a means for the characterization of the surface chemistry of adsorbents is the study of the infrared spectra of adsorbed carbon dioxide; since it is a small weakly interacting probe molecule very useful for the study of the acids and basics properties of solid surfaces [77–83]. In this regard, the adsorption interaction between the carbon dioxide molecule and the composite surface was studied with the help of the DRIFTS spectra of carbon dioxide adsorbed on the tested SWCNT–magentite-1 composite surfaces at 300 K. In Fig. 10 and Table 6 were reported the obtained data. This spectrum showed that the carbon dioxide molecule had direct interactions with the surface of the composite; because of the presence of three peaks in the detected experimental absorption band. These peaks were evidenced by fitting the experimental carbon dioxide infrared absorption band with the help of Lorentz functions.

In general, the free carbon dioxide molecule belongs to the $D_{\infty h}$ group of symmetry; showing four fundamental vibration modes, that is: the symmetric stretching, $v_1$(1338 $cm^{-1}$) the doubly degenerate bending vibration, $v_{2a}$ and $v_{2b}$ (667 $cm^{-1}$), and the asymmetric stretching vibration $v_3$ (2349 $cm^{-1}$) [64,77]. The $v_2$ and $v_3$ modes are infrared active, whereas $v_1$ is only Raman active, in the free molecule [78]. However, when a carbon dioxide molecule interacts with a surface it is not more a free molecule, and its symmetry is lowered, as a result the $v_1$ mode becomes infrared active, and a small band is observed, whereas the other modes undergo moderate changes in the wave number [78–80].

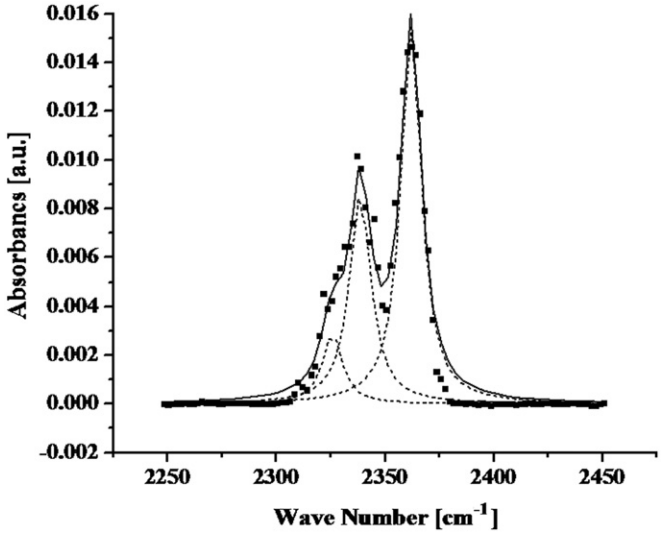


**Fig. 10.** DRIFTS spectrum of carbon dioxide adsorbed at 300 K on the SWCNT–magnetite-1 composite.

**Table 6**
Resolved peaks positions.

| Sample | $x_c^1$ ($cm^{-1}$) | $A_1$ (%) | $x_c^2$ ($cm^{-1}$) | $A_2$ (%) | $x_c^3$ ($cm^{-1}$) | $A_3$ (%) |
|---|---|---|---|---|---|---|
| SWCN-$Fe_3O_4$ | 2326 | 10.2 | 2339 | 33.7 | 2362 | 56.1 |

In Fig. 10 and Table 6 was clearly evidenced that the asymmetric stretching vibration, $v_3$, of the adsorbed carbon dioxide molecule was observed at around 2339 $cm^{-1}$. This band corresponds to carbon dioxide physically adsorbed inside the composite [81]. It is the result of the attachment of the carbon dioxide molecule by dispersive and electrostatic forces to the adsorption space of the magnetite particles defined by the magnetite and the carbon nanotube surfaces. The smaller band at about 2326 $cm^{-1}$, is normally assigned to a combination band related to the 2339 $cm^{-1}$ band [80,82].

Additionally, was observed another band at around 2362 $cm^{-1}$. In relation to this band it is possible to state that in the study of the adsorption of carbon dioxide on zeolites is very well documented the formation of weakly bonded adducts between the carbon dioxide molecule and the charge compensating cations, $M^+$, as follows, $M^{+\bullet\bullet\bullet\delta-}O{=}C{=}O^{\delta-}$ [79,80,82]. Furthermore, in a study of the adsorption of carbon dioxide in the molecular organic framework (MOF), MIL-100 [84], was found a $v_3$ band at 2351 $cm^{-1}$ that was assigned to the following species: $Cr^{3+\bullet\bullet\bullet}O{=}C{=}O$. Therefore, in our case the band at 2362 $cm^{-1}$ should characterizes the interaction of the carbon dioxide molecule with the coordinatively unsaturated cationic (cus) iron located in the surface of the magnetite core nanoparticles forming the following adducts: $Fe^{3+\bullet\bullet\bullet}O{=}C{=}O$ and $Fe^{2+\bullet\bullet\bullet}O{=}C{=}O$. This fact corroborates the Mössbauer spectrometry data.

Thus, since the bands at 2339 and 2326 $cm^{-1}$, that were previously related with the interaction of the carbon dioxide molecule with the dispersive and electrostatic forces, are weaker than the band at 2362 $cm^{-1}$ (see Table 6). Then, this fact indicates a significant interaction of the carbon dioxide molecule with the acid Lewis sites. Since, dispersive and electrostatic forces normally contribute to the isosteric heat of adsorption, $q_{iso}$ [11,12], in highly dispersed oxides, like silica about, $q_{iso} \approx 24$ kJ/mol, with a similar contribution for each interaction, i.e., $q_{iso} \approx 12$ kJ/mol [85]. Thereafter, the contribution of the interaction of the carbon dioxide molecule with the acid Lewis sites could be estimated as, $q_{iso} > 12$ kJ/mol.

## 4. Conclusions

The careful investigation of the morphologies of the single walled carbon nanotube, magnetite nanoparticles, and the composite prepared with these materials was performed with a rational combination of: X-ray diffraction, Raman spectroscopy, scanning electron microscopy, field emission scanning electron microscopy, high resolution transmission electron microscopy, nitrogen adsorption, thermogravimetric analyses and diffuse reflectance infrared transform spectroscopy. These methodologies, in conjunction, established that during the synthesis process, were produced pure single phases, that the SWCNTs exhibited high specific surface area, developed microporosity and homogeneous pore size, the magnetite cores of the capped material showed large specific surface area and high dispersion and that the composite material consisted of highly dispersed magnetite nanoparticles attached to the outer surface of the SWCNT.

The Mössbauer spectroscopy study demonstrated the existence of a large quantity of Lewis acid sites in the surface of the extremely dispersed magnetite particles supported on the SWCNT outer surface. The DRIFTS investigations of the composites under carbon dioxide adsorption applied as a probe molecule determined a significant interaction of carbon dioxide with the magnetite nanoparticles surface, largely in the Lewis sites. Therefore, the Lewis acid sites included in the high specific surface area of the magnetite nanoparticles were observed to be catalytically active. Additionally, the electron exchange between the Lewis acid sites and the basic or amphoteric adsorbed molecules might affect the magnetic properties of the magnetite nanoparticles during adsorption. Consequently, this investigation revealed the potential of the synthesized composites for catalytic and sensors applications.

Together with all the previously reported results, as far as we know, this is the first ever application of Mössbauer spectrometry in the study of Lewis acid sites

## Acknowledgments

The authors Francisco Marquez-Linares, Ramon Polanco, Carlos Neira, Santander Nieto and Rolando Roque-Malherbe, acknowledges the financial support provided by provided by the US Department of Energy through the Massey Chair project at University of Turabo. Additionally, the authors, Oswald N.C. Uwakweh and Neshma Lopez, acknowledges the support of NSF-DMRPREM at UPRM on Grant No. 0351449. The authors also acknowledge the collaboration of the Department of Physics and the Materials Characterization Center of the University of Puerto Rico, Rio Piedras Campus.

## References

[1] A. Corma, Chem. Rev. 95 (1995) 559.
[2] H. Hattori, Chem. Rev. 95 (1995) 537.
[3] H. Knözinger, S.J. Huber, J. Chem. Soc., Faraday Trans. 94 (1998) 2047.
[4] A. Zecchina, G. Spoto, S. Bordiga, Phys. Chem. Chem. Phys. 7 (2005) 1627.
[5] J.F. Haw, Phys. Chem. Chem. Phys. 4 (2005) 5431.
[6] M.G. Cutrufello, I. Ferino, R. Monaci, E. Rombi, G. Colo, J.A. Navio, Phys. Chem. Chem. Phys. 3 (2005) 2928.
[7] A. Corma, H. Garcıa, F.X. Llabres i Xamena, Chem. Rev. 110 (2010) 4606.
[8] D.M. Ruthven, F. Shamsuzzaman, K.S. Knaebel, Pressure Swing Adsorption, John Wiley and Sons, New York, 1994.
[9] R.T. Yang, Adsorbents: Fundamentals and Applications, J. Wiley and Sons, New York, 2003.
[10] S. Ernst (Ed.), Elsevier, Amsterdam, The Netherlands, 2009 vol. 1.
[11] R. Roque-Malherbe, Adsorption and Diffusion in Nanoporous Materials, CRC Press, Boca Raton, Florida, 2007.
[12] R. Roque-Malherbe, The Physical Chemistry of Materials: Energy and Environmental Applications, CRC Press, Boca Raton, Florida, 2009.
[13] H. Phillips, Hyperfine Interactions 111 (1998) 3.
[14] Z.Y. Zhong, T. Prozorov, I. Felner, A. Gedanken, J. Phys. Chem. B 103 (1999) 947.
[15] L. Stievano, S. Calogero, F.E. Wagner, S. Galvagno, C. Milone, J. Phys. Chem. B 103 (1999) 9545.
[16] M. Hartmann, L. Kevan, Chem. Rev. 99 (1999) 635.
[17] A. Zwijnenburg, A. Goossens, W.G. Sloof, M.W.J. Craje, A.M. van der Kraan, L.J. de Jongh, M. Makkee, J.A. Moulijn, J. Phys. Chem. B 106 (2002) 9853.
[18] J.-M. Millet, H. Knö1zinger, P. Bonville, J. Phys. Chem. B 110 (2006) 16003.
[19] J. Basak, N. Hardia, S. Saxena, R. Dixit, R. Dwivedi, S. Bhadauria, R. Prasad, Ind. Eng. Chem. Res. 46 (2007) 7039.
[20] K. Lazar, T. Mathew, Z. Koppany, J. Megyeri, V. Samuel, S.p. Mirajkar, B.S. Rao, J. Guczi, Phys. Chem. Chem. Phys. 4 (2002) 3530.
[21] H.A. Wiatrowski, S. Das, R. Kukkadapu, E.S. Ilton, T. Barkay, N. Yee, Environ. Sci. Technol. 43 (2009) 5307.
[22] K.R.P.M. Rao, F.E. Huggins, G.P. Huffman, R.J. Gormley, R.J. O'Brien, B.H. Davis, Energy Fuels 10 (1996)546 10 (1996).
[23] P.M. Ajayan, Chem. Rev. 99 (1999) 1787.
[24] M.A. Pimenta, G. Dresselhaus, M.S. Dresselhaus, L.G. Cançado, A. Jorio, R. Saito, Phys. Chem. Chem. Phys. 9 (2007) 1276.
[25] F. Marquez, C. Morant, J.M. Sanz, E. Elizalde., J. Nanosci. Nanotechnol. 9 (2009) 3810;
F. Marquez, C. Morant, J.M. Sanz, E. Elizalde., J. Nanosci. Nanotechnol. 9 (2009) 6127.
[26] F. Marquez, V. López, C. Morant, R. Roque-Malherbe, C. Domingo, E. Elizalde, F. Zamora, J. Nanomaterials (2010) Article ID: 189214, 7 pp. doi:10.1155/2010/189214.
[27] E. Poirier, R. Chahine, P. Benard, D. Cossement, L. Lafi, E. Melancon, T.K. Rose, S. Desilets, Appl. Phys. A 78 (2004) 961.
[28] D. Tasis, N. Tagmatarchis, A. Bianco, M. Prato, Chem. Rev. 106 (2006) 1105.
[29] M. Prato, K. Kostarelos, A. Bianco, Acc. Chem. Res. 41 (2008) 60.
[30] J.M. Tang, K. Jensen, M. Waje, W. Li, P. Larsen, K. Pauley, Z. Chen, P. Ramesh, M.E. Itkis, Y. Yan, R.C. Haddon, J. Phys. Chem. C 111 (2007) 17901.
[31] A.D. Lueking, R.T. Yang, Appl. Catal. A: Gen. 265 (2004) 259.
[32] C. Wang, M. Waje, X. Wang, J.M. Tang, R.C. Haddon, Y. Yan, Nano Lett. 4 (2004) 345.
[33] X. Wang, M. Waje, Y. Yan, Electrochem. Solid-State Lett. 8 (2005) A42.
[34] G. Girishkumar, T.D. Hall, K. Vinodgopal, P.V. Kamat, J. Phys. Chem. B 110 (2006) 107.
[35] Y. Yao, G. Li, S. Ciston, R.D. Lueptow, K.A. Gray, Environ. Sci. Technol. 42 (2008) 4952.
[36] F. Rodriguez-Reinoso, A. Sepulveda-Escribano, in: H.S. Nalwa (Ed.), Handbook of Surfaces and Interfaces of Materials, vol. 5, Academic Press, New York, 2001, p. 309.
[37] Y. Wang, N. Shah, F.E. Huggins, G.P. Huffman, Energy Fuels 20 (2006) 2612.
[38] J.E. Trancik, S.C. Barton, J. Hone, Nano Lett. 8 (2008) 982.
[39] Z. Kang, E. Wang, B. Mao, Z. Su, L. Gao, L. Niu, H. Shan, L. Xu, Appl. Catal. A: Gen. 299 (2006) 212.
[40] Q. Li, L. Chen, G. Lu, J. Phys. Chem. C 111 (2007) 11494.
[41] R.M. Cornell, U. Schwertmann, The Iron Oxides: Structure, Properties, Reactions, Occurrence and Uses, VCH, New York, 1996.
[42] L.X. Tifenauer, A. Tschirky, G. Kuhne, R.Y. Andres, Magn. Reson. Imaging 14 (1996) 391.
[43] V.G. Roullin, J.R. Deverre, L. Lemaire, F. Hindre, M.C.V. Julienne, R. Vienet, J.P. Benoit, Eur. J. Pharm. Biopharm. 53 (2002) 293.
[44] S. Si, A. Kotal, T.K. Mandal, S. Giri, H. Nakamura, T. Kohara, Chem. Mater. 16 (2004) 3489.
[45] E. Lima Jr., A.L. Brandl, A.D. Arelaro, G.F. Goya, J. Appl. Phys. 99 (2006) 083908.
[46] G. Gnanaprakash, J. Philip, T. Jayakumar, B. Raj, J. Phys. Chem. B 111 (2007) 7978.
[47] T. Atarashi, T. Imai, J. Shimoiizaka, J. Magn. Magn. Mater. 85 (1990) 3.
[48] P. Roonasy, Licenciate Thesis, Department of Chemical Engineering and Geosciences, Division of Chemistry, Lulea University of Technology, Lulea, 2007.
[49] J.M. Thomas, W.J. Thomas, Principle and Practice of Heterogeneous Catalysis, VCH Publishers, New York, 1997.
[50] G.A. Somorjai, Introduction to Surface Chemistry and Catalysis, John Wiley & Sons, New York, 1994.
[51] B.A. Averil, J. Moulijn, P.W.N.M. Van Leuwen, R.A.Van Santen (Eds.), second edn., Elsevier, Amsterdam, , 2000.
[52] J.A. Lercher, C. Gründling, G. Eder-Mirth, Catal. Today 27 (1996) 353.
[53] M. Rodrıguez-Delgado, C. Morterra, G. Cerrato, G. Magnacca, C. Otero-Arean, Langmuir 18 (2002) 10255.
[54] G.F. Goya, T.S. Berquo, F.C. Fonseca, M.P. Morales, J. Appl. Phys. 94 (2003) 3520.
[55] J. Korecki, B. Handke, N. Spiridis, T. Slezak, I. Flis-Kabulska, J. Haber, Thin Solid Films 412 (2002) 14.
[56] S. Morup, H. Topsoe, J. Lipka, J. Phys. 12 (1976) C6.
[57] M.F. Thomson, C.E. Johnson, in: D.P. Dickson, F.J. Berry (Eds.), Mössbauer Spectroscopy, Cambridge University Press, Cambridge, 1986, p. 143.
[58] D. Szabo, I. Czako-Nagy, M. Zrınyi, A.C. Vertes, J. Coll. Interf. Sci. 221 (2000) 166.
[59] S. Laurent, D. Forge, M. Port, A. Roch, C. Robic, L. Vander Elst, R.N. Muller, Chem. Rev. 108 (2008) 2064.
[60] J. Wielant, T. Hauffman, O. Blajiev, R. Hausbrand, H. Terryn, J. Phys. Chem. C 111 (2007) 13177.
[61] A. Dixit, Ph. D. Dissertation, University of Puerto Rico, Rio Piedras, PR, 2003.
[62] D.G. Rancourt, J.Y. Ping, Nucl. Instr. Methods 58 (1991) 85.
[63] B.D. Cullity, S.R. Stock, Elements of X-ray Diffraction, third edn., Prentice Hall, Upper Saddle River, NJ, 2001.
[64] K. Nakamoto, Infrared and Raman Spectra of Inorganic and Coordination Compounds: Part A: Theory and Applications in Inorganic Chemistry, J. Wiley & Sons, New York, 1997 vol. 1.
[65] Y. Liu, C. Pan, J. Wang, J. Mater. Sci. 39 (2004) 1091.
[66] R. Bonadiman, M.D. Lima, M.J. de Andrade, C.P. Bergmann, J. Mater. Sci. 41 (2006) 7288.
[67] A. Jorio, R. Saito, J.H. Hafner, C.M. Lieber, M. Hunter, T. McClure, G. Dresselhaus, M.S. Dresselhaus, Phys. Rev. Lett. 86 (2001) 1118.
[68] Y. Mi, Y. Liu, D. Yuan, J. Zhang, Y. Xiao, J. Mater. Sci. 40 (2005) 3635.
[69] L.V. Gasparov, D.B. Tanner, D.B. Romero, H. Berger, G. Margaritondo, L. Forro, Phys. Rev. B 62 (2000) 7939.
[70] I. Chourpa, L. Douziech-Eyrolles, L. Ngaboni-Okassa, J.-F. Fouquenet, S. Cohen-Jonathan, M. Souce, M. Marchais, P. Dubois, Analyst 130 (2005) 1395.
[71] Y. Xiong, J. Ye, J.X. Gu, Q.-W. Chen, J. Phys. Chem. C 111 (2007) 6998.
[72] M. Gotic, S. Music, J. Mol. Struct. 834–836 (2007) 445.
[73] M. Yamauraa, R.L. Camiloa, L.C. Sampaiob, M.A. Macedoc, M. Nakamurad, H.E. Toma, J. Magn. Magn. Mater. 279 (2004) 210.

[74] D. Satula, D.B. Kalska-Szostko, K. Szymanski, L. Dobrzynskia, J. Kozubowski, Acta Phys. Polonica A 114 (2008) 1615.
[75] U. Gonser, H.D. Pfannes, J. Phys. 35 (1974) C6–113.
[76] H.D. Pfannes, U. Gonser, Appl. Phys. 1 (1973) 93.
[77] A.L. Goodman, L.M. Campus, K.T. Schroeder, Energy Fuels 19 (2005) 471.
[78] B. Bonelli, B. Onida, B. Fubini, C. Otero-Arean, E. Garrone, Langmuir 16 (2000) 4976.
[79] H. Knozinger, S. Huber, J. Chem. Soc., Faraday Trans. 94 (1998) 2047.
[80] F.X. Llabres i Xamena, A. Zecchina, Phys. Chem. Chem. Phys. 4 (2002) 1978.
[81] A.L. Goodman, Energy Fuels 23 (2009) 1101.
[82] B. Bonelli, B. Civalleri, B. Fubini, P. Ugliengo, C. Otero Arean, E. Garrone, J. Phys. Chem. B 104 (2000) 10978.
[83] J.C. Lavalley, Catal. Today 27 (1996) 377.
[84] P.L. Llewellyn, S. Bourrelly, C. Serre, A. Vimont, M. Daturi, G. LHamon, J.-S. De Weireld, D.-Y. Chang, Y.K. Hong, S.H. Hwang, G.Ferey Jhung, Langmuir 24 (2008) 7245.
[85] R. Roque-Malherbe, R. Polanco, F. Marquez-Linares, J. Phys. Chem. C 114 (2010) 17773.